Quantification and 3D Localization of Magnetically Navigated Superparamagnetic Particles Using MRI in Phantom and Swine Chemoembolization Models

Digital Object Identifier 10.1109/TBME.2022.3151819

Ning Li
Cyril Tous
Ivan P. Dimov
Dominic Cadoret
Phillip Fei
Yasamin Majedi
Simon Lessard
Zeynab Nosrati
Katayoun Saatchi
Urs O. Häfeli
An Tang
Samuel Kadoury
Sylvain Martel, Fellow, IEEE
Gilles Soulez

Ning Li, Cyril Tous, Ivan P. Dimov, Dominic Cadoret, Phillip Fei, Simon Lessard, and An Tang are with the Laboratoire clinique du traitement de l'image, Centre de recherche du Centre Hospitalier de l'Université de Montréal (CRCHUM), Canada.
Yasamin Majedi, Samuel Kadoury, and Sylvain Martel are with the De- partment of Computer and Software Engineering, Institute of Biomedical Engineering, Polytechnique Montréal, Canada.

Zeynab Nosrati, Katayoun Saatchi, and Urs O. Häfeli are with the Faculty of Pharmaceutical Sciences, University of British Columbia, Canada.

Gilles Soulez is with the Laboratoire clinique du traitement de l'image, Centre de recherche du Centre Hospitalier de l'Université de Montréal (CRCHUM), Montréal, QC H2X 0A9, Canada, with the Department of Radiology, Centre Hospitalier de l'Université de Montréal (CHUM), Montréal, QC H2X 0C1, Canada, and also with the Department of Radi- ology, Radiation Oncology and Nuclear Medicine, University of Montréal, CP 6128, Succ. Centre-ville Montréal, Montréal, QC H3T 1J4, Canada (e-mail: gilles.soulez.med@ssss.gouv.qc.ca).

Index Terms—Quantification and localization, magnetic drug-eluting beads, particle number, spatial locations, sus- ceptibility artifact, 3D volumetric interpolated breath-hold examination.

This work was supported in part by a grant from the Canadian Institute of Health Research (CIHR 202003PJT-437727-MPI-ADWY-19089), in part by Fonds de recherche du Québec en Santé (FRQS) and Fondation de l'association des radiologistes du Québec (FARQ) Clinical Research Scholarship under Grant 34939, and in part by Transmedtech and Siemens Healthineers. The work of Urs O. Häfeli was supported by the Lundbeck Foundation of Denmark through UBC-SUND Lundbeck Foundation Professorship under Grant 2014-4176. (Corresponding author: Gilles Soulez.)

Abstract

Objective: Superparamagnetic nanoparticles (SPIONs) can be combined with tumor chemoemboliza- tion agents to form magnetic drug-eluting beads (MDEBs), which are navigated magnetically in the MRI scanner through the vascular system. We aim to develop a method to accurately quantify and localize these particles and to validate the method in phantoms and swine models. Meth- ods: MDEBs were made of Fe_3O_4 SPIONs. After injected known numbers of MDEBs, susceptibility artifacts in three- dimensional (3D) volumetric interpolated breath-hold ex- amination (VIBE) sequences were acquired in glass and Polyvinyl alcohol (PVA) phantoms, and two living swine. Image processing of VIBE images provided the volume relationship between MDEBs and their artifact at different VIBE acquisitions and post-processing parameters. Sim- ulated hepatic-artery embolization was performed in vivo with an MRI-conditional magnetic-injection system, using the volume relationship to locate and quantify MDEB distri- bution. Results: Individual MDEBs were spatially identified, and their artifacts quantified, showing no correlation with magnetic-field orientation or sequence bandwidth, but ex- hibiting a relationship with echo time and providing a lin- ear volume relationship. Two MDEB aggregates were mag- netically steered into desired liver regions while the other 19 had no steering, and 25 aggregates were injected into another swine without steering. The MDEBs were spatially identified and the volume relationship showed accuracy in assessing the number of the MDEBs, with small errors (≤ 8.8%). Conclusion and Significance: MDEBs were able to be steered into desired body regions and then localized using 3D VIBE sequences. The resulting volume relationship was linear, robust, and allowed for quantitative analysis of the MDEB distribution.

I. INTRODUCTION

NTELLIGENT micro/nanorobotic systems-based naviga- tion techniques, capable of directing micro-and nanorobotic agents to targeted areas, have obtained considerable attention in the biomedical field [1]–[3]. Over the last decade, impressive progress has been made in designing microrobots, their propul- sion mechanisms, and microrobot-tracking techniques [4]–[9]. However, some challenging issues that prevent microrobots from being deployed in vivo still exist [10], [11]. For example, to improve patient survival after chemoembolization of hepatocel- lular carcinomas, selective embolization at the segmental level is now the recommended practice. If an implantable catheter is positioned in the proper hepatic artery, microrobots must be navigated across two bifurcations before reaching the targeted segments in the left lobe of the liver or three bifurcations before arriving at the targeted segments in the right lobe [12]. Thus, there is a strong clinical interest to achieve accurate quantifica- tion and three-dimensional (3D) localization of microrobots to improve tumor targeting and minimize non-target embolization. Significant progress has recently been made to track/image micro and nanoscale objects during or after targeted operations. Hong et al. successfully achieved real-time 3D position tracking of microrobots using digital holography (optical method) [13]. Vilela et al. demonstrated that positron emission tomography is a suitable technique for visualizing the movements of micro- robots in real-time in opaque environments [10]. Olson et al. proposed to track microrobots by detecting hydrogen peroxide with ultrasound molecular imaging [14].

However, such imaging techniques still face some technical difficulties due to their imaging principles. Optical methods have a low capacity for penetrating biological tissues and are only applicable in superficial layers [13]. Nuclear techniques, such as positron emission tomography or single-photon emis- sion computed tomography, can identify small particles in deep tissues but rely on harmful gamma rays [10]. Ultrasound imaging can only be used to track micro/nanorobots moving via the bubble-propulsion mechanism because its resolution depends on both the gradients in acoustic impedance and the structures larger than the sonographic detection limit [14]. Moreover, the imaging techniques mainly focus on the tracking of micro and nanoscale objects during targeted operations but not on accu- rately quantifying and localizing them.

Magnetic drug-eluting beads (MDEBs), a type of drug-eluting microrobots made of superparamagnetic nanoparticles (SPI- ONs) and loaded with anti-tumor drugs, may be used to address the challenge through the susceptibility artifact phenomenon visible on MR images [15]–[17]. MDEBs can be selectively navigated across one or several vascular bifurcations to en- ter tumor areas by using different magnetic actuators and/or techniques, such as multi-degree-of-freedom superconducting coils and magnetic resonance navigation (MRN) [18]–[20]. The inclusion of Fe3O4 SPIONs into MDEBs has been proposed to target hepatocellular carcinomas or visualize particle distribu- tions after MRI-based embolization procedures, without adding the radioactive compounds that are required in positron emission tomography–computed tomography [21], [22].

Most proposed techniques for imaging MDEBs used T2-or T2∗-weighted MR sequences [21], [23]. MRN is now possible by creating MDEB aggregates after using a dedicated injector [24]. The formed ag- gregates composed of tens of MDEBs can be visible in real-time 2D True FISP sequences which have a signal intensity related to T2 over T1 contrast and not T2∗ [20]. Using a 2D multi-echo gradient echo sequence (GRE) and T2∗ measurements, Kim et al. found a good correlation between signal loss and particle concentration made of iron oxide nanoparticles in rat models in vitro and in vivo [25]. In a rabbit model, Pouponneau et al. used a T2∗-weighted GRE sequence to analyze the particle distribution ratios in the left and right liver lobes following MRN [26]. A good correlation between FeCo volume and signal loss volumewas obtained.

However, only the exit of the catheter can be visualized when using 2D sequences because of the limited volume coverage [20]. The susceptibility artifact obtained using the T2∗ sequence was too large to discriminate individual aggregates in different liver lobes [15], [26]. In addition to the limitations above, T2 and T2∗ measurements also require a long scanning time. In the study carried out by Pouponneau et al., the slice number was only set to 4 and each slice needed 8 s in the rabbit model [26]. In the human liver, at least 70 slices are needed to cover the whole liver if the slice thickness is set to 3 mm. In a study of ferromagnetic artifacts by Chiba et al. the acquisition time (TA) of T2- and T2∗-weighted sequences were three to four times longer than the T1-weighted sequences [27]; T1 needs 10 seconds to 1 minute while the other two sequences demand more than 2 minutes which is not compatible with a breath-hold. Even if now, T2∗ acquisitions can be acquired within a breath-hold, the T2∗ and T2 weighted images depict dark liver contrast, which further impairs our ability to distinguish signal loss from the particles with dark signals from the liver on the T2 or T2∗ weighted images.

In the case of chemoembolization for hepatocellular carcino- mas patients, knowing the required number of MDEBs would optimize treatments and minimize tissues at risk. Therefore, we aim to establish the relationship between artifact volume and MDEB volume when the MDEBs are in the range of 0.1 to 1 mm in diameter [24], [28]. Susceptibility artifacts induced by magnetic materials consist of three components: the material itself, the static magnetic field, and the magnetic field distor- tions in the vicinity of magnetic materials [29]. Generally, the artifact size is determined by the difference in susceptibilities (Δ Susceptibility), magnetic field strength (B0), echo time (TE) as well as bandwidth (BW) (or readout gradient strength and direction) [29], [30].

$$\text{artifact size} \propto ((\Delta \text{ Susceptibility}) \cdot B0 \cdot TE) / BW \quad (1)$$

We also require serial fast high-resolution 3D acquisitions to accurately localize and count the MDEB aggregates in liver segments. The volumetric interpolated breath-hold examination (VIBE) sequence, a radio-frequency-spoiled 3D GRE sequence, has been effectively used in abdominal and breast imaging. Contrast-enhanced VIBE imaging has been routinely used for liver lesion detection and characterization [31]. The “breath- hold”

acquisitions typically require less than 30 seconds to obtain dynamic, high-resolution T1-weighted tissue imaging [32], [33].

This paper evaluates the possibility of accurately quantifying and localizing MDEBs in the body using a breath-hold volumet- ric acquisition. This would allow near real-time assessments of tumor-targeting efficiency. The MDEBs used in our experiments were made from a poly (lactic-co-glycolic acid) (PGLA) poly- mer matrix embedded with C12-bisphosphonate coated Fe3O4 SPIONs.

II. METHOD

A. Theory

For a large magnetic object, the relationship between its true volume and MRI artifact volume, as selected within the region of signal dropout caused by the object (Fig. 1), is given in Eq. (1) above. This relationship can be simplified to the linear equation:

$$VA = av \qquad (2)$$

where VA is the artifact volume, v represents the object volume, and $a \propto ((\Delta \text{ Susceptibility}) \cdot B0 \cdot TE)/BW$ is the constant ratio determined by the imaging parameters (BW, TE, B0) defined in Eq. (1).

However, for microparticle-based artifacts, the interference effect caused by the background signal intensity must be con- sidered. Different tissues/materials will have different baseline signal intensities and the segmentation volume may depend in practice on this signal intensity. For example, compared with Fig. 1(a), (b) has a weaker background signal intensity around the magnetic microparticle. An additional segmentation artifact volume b can be selected if we used the same segmentation threshold. Hence,

$$VA = av + b \qquad (3)$$

B. Equipment and Materials

To test our hypothesis, the parameters a and b in Eq. 3 were experimentally validated in a 3T MRI scanner (Skyra, Siemens, Erlangen, Germany). As shown in Fig. 2, the MDEBs (200 ± 12 µm; coefficient of variation = 6%) used in the experiments were composed of Fe3O4 SPIONs (12 ± 3.6 nm) coated with C12-bisphosphonate and poly(lactic-co-glycolic) acid (PLGA) (50:50 ester terminated; MW 60−100 kDa; IV 0.76−0.94 dL/g, Durect Co., AL, USA) in a co-precipitation method [34], [35].

The microparticle size and its composition met biocompatibility requirements for liver embolization [28], [36]–[39]. Further- more, the MDEBs are biocompatible with kidney and endothe- lial cells [40]. Their saturation magnetization reached 30 emu/g (≥1.5 T) (vibrating sample magnetometer EV9, Microsense). For this set of experiments, the MDEBs were not loaded with

drugs to reduce costs and facilitate manipulation. A symmetric transparent glass phantom (custom-made by Cédric Ginart Company in Montreal, Canada) and a PVA phantom were built to mimic the hepatic arterial tree, as shown in Fig. 2(d) and (e).
The influence of the MR imaging parameters (BW, TE, B0) on a (Eq. (3)) was tested in the glass phantom. Then, to validate b , the PVA phantom was used since its material (composition: [CH2CH(OH)]n; density: 1.19-1.31 g/cm3) has a proton density (about 0.108-0.119 mol/cm3) similar to water (0.111 mol/cm3) and soft tissues. Thus, PVA was expected to have the background signal intensity equal to or greater than that of water, resulting ina lower b compared with that in the glass phantom.

Finally, the MDEB aggregates were localized and quantifiedin the livers of two 40 kg white domestic swine, which was approved by the CHUM Research Center's Institutional Animal Care Committee (C17014GSp).

C. Dependence on the MRI Sequences

To select a proper MR imaging sequence for quantifying and localizing the MDEB aggregates, we considered two main criteria: the acquisition time (TA) and the corresponding arti- fact size. To minimize the artifact misregistration induced by respiratory motion, we need a volumetric sequence with a short TA compatible with the breath-hold that ensures good spatial resolution. Gay et al. evaluated the breath-holding capabilities of various groups of individuals and the results revealed that 1) the maximum breath-hold time for some patients (heavy smok- ers, and patients with chronic obstructive pulmonary disease or congestive heart failure) was 18 s to 32 s (95% confidence interval) with a mean of 25 s; 2) for all other outpatients, the time was 38 s to 56 s (mean = 45 s) [41]. Therefore, when the proper sequence and corresponding imaging parameters were selected, TA was expected to be within 20 s. Regarding the artifact size, many large artifacts induced by adjacent MDEB aggregates may overlap with each other thus limiting aggregate quantification and localization [26], [27].

D. Reconstruction of Artifact Volume

After MR imaging of the MDEB aggregates, the original MR images were directly loaded into the post-processing software (3D-Slicer) to analyze the susceptibility artifact volume through a manual slice-by-slice segmentation process [42]. The win- dow/level (W/L) setting [43] of the post-processing software was manually tuned to have an ideal visualization effect: the glass phantom was tuned to be invisible while the MDEB artifact could still be identified clearly. Then, the threshold value set in the software was determined to automatically select the artifact areas with complete coverage. The threshold operation enabled us to select ranges of grayscale pixel values. After selecting the artifact area, the 3D artifact model was built automatically.

The segment statistics function built into the post-processing software was used to calculate the number (Ns) of the segmented voxels. The VA in Eq. 3 can be calculated as:

$$VA = Ds \cdot Ns \cdot Ps2 \qquad (4)$$

where Ds and Ps represent the slice thickness and the pixel spacing, respectively. The slice gap is null in a T1 VIBE acquisition. Thus, we can assess how Ns changes with fixed and varying parameters due to either the sequence (BW, slice thick- ness, etc.) or the post-processing (W/L and threshold values). In our experiments, the MDEBs have a relatively uniform size (coefficient of variation = 6%), so their number is proportional to their volume. In fact, Eq. (3) expresses the relationship between the artifact voxel count and the particle count (AVC-PC).

E. Preparation of the In Vitro Experiments

Particle aggregates with known numbers (10–100) of particles were injected into the glass and PVA phantoms to validate our hypothesis in Section II-A. The two phantoms were placed in a separate rectangular box (50 cm × 30 cm × 30 cm) filled with water. A vinyl tubing (1.09 mm internal diameter) was inserted into their main branches. The MDEBs were manually counted in a small tubing, injected into the main branches of the phantoms, and trapped with a cylindrical neodymium magnet (1.6 mm diameter × 1.6 mm thickness) to form an aggregate. Finally, the phantoms were placed at the MRI iso-center.

F. Animal Preparation

Two swine were under general anesthesia throughout the experiment and were euthanized at the end. Catheter insertion was performed in the experimental angiography room (Artis Q, Siemens, Forchheim, Germany). An experimental gel made of chitosan-sodium tetradecyl sulfate was used to embolize the right gastric artery (0.5 ml gel) and the gastroduodenal artery (1.5 ml gel) [44]. Rotational digital subtraction angiography (DSA) was performed to obtain the 3D model of the liver arterial system. A 5 Fr balloon catheter (Powerflex P3, Cordis, USA) was placed 3 to 4 cm below the first bifurcation linking the left and right hepatic arteries. Then, they were transferred to the 3T MRI room (Skyra, Siemens, Erlangen, Germany). Magnetic Resonance Angiography (MRA) was acquired with a T1-weighted gradient-recalled sequence (TR = 3.33 ms, TE = 1.23 ms, FA = 19°, FOV = 300 mm, 0.78 mm in-plane isotropic voxel, and 0.8 mm slice thickness) during a breath-hold after intravenous injection of 0.5 mmol/kg of gadolinium (Prohance, Bracco Imaging, Anjou, Quebec). Then, the guidewire lumen port of the catheter was connected to our MRI-compatible injector to allow for the injection of the MDEB aggregates [24]. Before MRN, swine#1 was rotated on its left side (see Fig. 3) to place the first vessel bifurcation in the horizontal plane to eliminate the influence of particle gravity on MRN. After balloon inflation, the blood flow rate in the proper hepatic artery was measured at ~ 0.3 ml/s using the 2D cine phase-contrast sequence (TR = 50.32 ms, TE = 3.61 ms, FA = 20°, FOV = 200 mm, voxel size = 0.39 mm × 0.39 mm × 3.70 mm, and VENC = 30 cm/s) under cardiac gating. Swine#2 was injected with particles without MRN and was kept in the supine position in the angiography and MRI rooms. A Terumo Radifocus Glidecath catheter (5Fr, Terumo, Tokyo, Japan) was used and yielded the blood flow of 6 ml/s measured by the 2D cine phase-contrast sequence (same parameters with changes on VENC = 60 cm/s). The embolization (right gastric artery and gastroduodenal artery), catheter insertion, DSA and MRA operations in the two swine were the same. When performing the T1-vibe sequence, the MR technician gave the veterinary nurse instruction

on when to stop the ventilation (a portable MRI-compatible ventilator (ModuFlex Compact Veterinary Anesthesia Machine, Dispomed, Joliette, Quebec, Canada) with an isoflurane vaporizer (InterMed Penlon Sigma Delta, United Kingdom)) during scan acquisition.

G. MRN Sequence

Our MRN sequence was based on the Echo Planar Read- out code and was programmed by the Integrated Development Environment for MR Applications (Siemens, Germany). The frequency encoding (left direction in Fig. 3) and phase encoding (up direction) gradients were used in the MRN sequence to steer MDEBs into the left hepatic arteries. Since the sequence is based on the Echo Planar Readout code which accounts for the gradient cooling, the MRI can sustain the nominal value for the steering duration. The gradient durations were 8 ms in the left and up direction for amplitudes of 26.5 mT/m and 18 mT/m, which yields a 32 mT/m nominal amplitude for 29.5% duty cycle given TR = 14 ms and Gmax = 43 mT/m [45]. In each MRN cycle, an MDEB aggregate was released from our injector and followed by the opening of the pre-set MRN sequence. The sequence would last 30 s for each MRN cycle.

H. Registration Between the DSA and MRA

The current resolution of the contrast-enhanced MRA (∼0.8 mm isotropic) does not provide enough resolution down to the segmental level of the arteries. We proposed to perform an elastic registration between the preoperative 3D DSA performed in the Angio Suite and the MRA acquired in the MRI room. The segmentation from MRA, with distinct main arteries but missing subsegmental arteries, was used as anatomical point landmarks for the thin plate spline elastic registration with the vascular segmentation from computed tomography angiography images with an affine deformation matrix [46]. The hepatic arterial trees from the MRA and DSA images were manually aligned to locate the particle aggregates in blood vessels.

I. Signal to Noise Ratio Analysis

The signal to noise ratio (SNR) values obtained from the MR images were analyzed both in vivo and in vitro using the method proposed by the National Electrical Manufacturers Association: in an MR image, a circular region of interest was selected to measure the mean signal S and four regions of interest were chosen at four corners (air) to determine the mean and standard deviation (SD) of the background noise [47], [48]. The SNR is the ratio of S by the standard deviation of the noise multiplied by 0.66 to account for the Rayleigh noise distribution.

III. EXPERIMENTS AND RESULTS

A. Dependence on the MR Imaging Sequences

Here, we compared MR visibility of the MDEBs in T1- weighted, T2∗-weighted spoiled GRE, and T2-weighted fast spin-echo sequences, with the following parameters: T1-VIBE sequence (out-of-phase: Repetition Time (TR) = 5.2 ms, TE = 1.4 ms; in-phase: TR = 5.2 ms, TE = 2.6 ms, Flip an- gle (FA) = 9°, Matrix size = 195 × 320, slice thickness = 3 mm, Field-of-

view (FOV) = 282 mm × 347 mm, BW = 1040 Hz, slice = 72), T2-weighted sequence (same parameters with changes on TR = 1660 ms, TE = 73 ms), and T2∗-weighted GRE sequence (same parameters with changes on TR = 215 ms, TE = 9 ms, slice = 52). T1-VIBE was acquired in 19 s which satisfies the breath-hold requirement while the T2 and T2∗ sequences required 1 min 50 s and 2 min, respectively. The empirically optimized imaging protocol parameters, especially including BW, slice thickness, in-plane pixel size and TA, were investigated and achieved using the user interface of the VIBE sequence on the scanner. Changing the BW from 1040 Hz to 1565 Hz decreased the TE from 1.4 ms to 1.2 ms and increased the voxel size from 1.1 mm × 1.1 mm × 3 mm to 1.6 mm × 1.6 mm × 3 mm while keeping FOV = 282 mm × 347 mm, and TA = 19 s. To maintain the 1 mm × 1 mm × 3 mm resolution and the BW at 1565 Hz, the FOV should be increased to 390 mm × 480 mm which increased the TA to 27 s. We also tested the TA with different slice thicknesses and pixel sizes in the range of 1-5 mm, as shown in Fig. 4. The scan volume was equal to the volume used in our in vivo experiments below. It is clear the voxel size = 1.1 mm × 1.1 mm× 3 mm is the most optimized parameter, which does not only ensure patient's reasonable breath-hold time but also the maximum resolution
that can be obtained within 20 s.

Regarding the artifact size, a single particle was clearly visible (see Fig. 5(a)) in the PVA phantom aggregates using the VIBE sequence without a large susceptibility artifact thus minimizing the overlapping risk between individual areas of signal loss.
Therefore, the T1-VIBE parameters above were defined as the default imaging parameters. The out-of-phase contrast images, in contrast to those of the in-phase, minimize artifact overlay and thus were used for analysis (see Fig. 5(b)).

B. Reconstruction of the Artifact Volume

Fig. 6 shows the reconstruction of an artifact induced by a 60-particles-based aggregate. The optimized W/L and threshold were 350/40 and [0-200], respectively (following the requirement from Section II-D).

C. In Vitro Experiments

Two factors may affect the AVC-PC relationship. The first factor includes several MRI parameters, such as B0, BW and TE (Eq. 1) and the geometric phantom orientation with B0. The second factor is the settings (threshold and W/L) of the post-processing software. After using the same MRI acquisition parameters (default imaging parameters, see Section III- A), the threshold values with an upper limit ranging between 140 and 200 were tested at W/L = 350/40 for all analyzed images.

As shown in Fig. 7(a), 1) the orientation of the glass phantom did not affect the AVC-PC relationship, and 2) the AVC-PC relationship obeyed Eq. 3 with an estimate of a = 3.59 and b = 70.4. The BW was not considered to affect the AVC-PC relationship (see Fig. 7(b)). Since the BW was shown to have no obvious impact on the AVC-PC relationship, we can conclude that the TE significantly affected it (Fig. 7(c)). In Fig. 7(d), the results reveal that:

1) a increased with the intensity threshold values, 2) the threshold level affected both a and b in the same proportion.

As shown in Fig. 8(a), a changed very slightly, from 3.59 (glass phantom) to 3.55 (PVA phantom) when the phantom was along and perpendicular to B0. Therefore, the parameter a in Eq.

(3) was validated. The parameter b, affected by the background signal intensity around the MDEBs, decreased from 70.5 (glass phantom) to 5.7 (PVA phantom), verifying our hypothesis about b in Eq. (3). Fig. 8(b) revealed again that: the threshold level set in the post-processing software affected a. In the threshold range [0, 200], a has the smallest difference (<1%) in the two phantoms.

D. Animal Study

For swine#1, 21 particle aggregates (25 ± 6 MDEBs per aggregate) formed by our injection system were injected through the catheter. The first two MDEB aggregates were applied with magnetic forces pointing to the left hepatic artery and the last 19 injections were done without MRN. For the aggregate fragments observed in the liver, we used labeling format (Fm-f) for them. The subscript m indicates the number of injections, and f marks each fragment after m times of aggregate injections.

Fig. 9(c) shows that the first injected MDEB aggregate broke into 5 aggregate fragments. The number of voxels with susceptibility artifacts was 68 (F1-1), 59 (F1-2), 64 (F1-3), 124 (F1-4) and 83 (F1-5) segmented voxels, respectively. According to Eq. 3, b should range between 58 (if 25 + 6 = 31 particles were injected) and 67 (if 25 - 6 = 19 particles were injected).

After the second injection, 4 aggregate fragments (F2-1, F2-2, F2-3 and F2-4) were found. From Fig. 9(c), F1-1 and F2-1 had a similar profile and artifact voxel count, as well as F1-2 and F2-2, or F1-5 and F2-4. In fact, they are the same particle or aggregate; the small misalignment can be explained by the difference of breath-hold amplitude between acquisitions. After the second injection, F1-3 and F1-4 aggregated together and formed the big aggregate F2-3. The aggregates F1-1, F1-2, and F1-5 had no change and were labeled again as F2-1, F2-2, and F2-4, respectively. The calculation results in Fig. 9(d) revealed that the total number of particles located in the liver increased by 20 after the second injection, based on Eq. (3), a = 3.6 and b = [58-67] (as described above). The increased number was just within the injection precision of our system (25 ± 6).

After 21 aggregate injections, 27 aggregate fragments with clear spatial locations and artifact volumes were identified (Fig. 9(a)). A total of 479 particles (see Fig. 10(b) and (c), calculated by Eq. (3), a = 3.6 and b = 60) were found in the liver, meaning that an average of 23 MDEBs had been injected per bolus (total number of injections = 21) which is within the precision range (25 ± 6) of the used injection system, yielding an estimation error less than 8% calculated by (25-23)/25.

Aggregate fragments were found in the areas located down- stream of the third-level bifurcations after manually embedding the hepatic arterial tree segmentation from the MRA and DSA images (for swine#1, see Fig. 11(b) and (c); for swine#2, see Fig. 12).
For swine#2, 25 aggregates (25 ± 6 MDEBs per aggregate) were injected and the T1-vibe sequence was executed every five injections. Fig. 12 shows the calculated particle count versus the theoretical MDEB injection count using the AVC-PC relationship obtained from swine#1. The result revealed that the calculated value was basically consistent with the theoretical value. A total of 680 particles (34 aggregate fragments) were found in the liver after the injections, yielding an estimation error of less than 8.8% calculated by (680-625)/680.

These results also revealed that T1-VIBE-based susceptibility artifacts are of sufficient resolution to localize aggregate fragments in the liver and count the number of their constituent particles. At the same time, we found that with finer vessel segmentation in the 3D slicer, smaller blood vessel branches were visible and most MDEB artifacts (31/34) were in the vicinity of blood vessels (see Fig. 12). It means that we can quickly and easily localize the blood vessels where the particles enter, as well as the liver lobes. Of course, finer segmentation requires longer post-processing times.

E. SNR Analysis

The resulting SNRs were 67.2 (glass wall), 400.2 (PVA phan- tom), 194.9 (water), 43.0 (artifact in the glass phantom) and 44.0 (artifact in the PVA phantom). The contrast-to-noise ratio of artifact-to-glass and artifact-to-PVA were thus 24.2 and 356.2. These results satisfy our hypothesis that b in the PVA phantom is smaller than b in the glass phantom because of the difference in proton density.

Before the MDEB injection during the in vivo experiment, the SNRs (mean of 8 measurements) were estimated at 174.1 ± 14.4 (mean ± SD) in the blood vessels, at 300.6 ± 29.8 in the adjacent liver tissues, and after particle injection at 56.1 ± 3.8 in the artifact area. The three values were studied at different liver segments; no obvious difference was found. The SNRs of the adjacent liver tissues beside the measured vessels and artifacts are within 5% of each other before and after the particle injection, which was not significantly different. Thus, the contrast-to-noise ratio between the artifacts and the surrounding liver tissues (no vessel) was 300.6 - 56.1 = 244.5.

IV. DISCUSSION

A. The MDEB and MRN

Embedding magnetic particles into MDEBs is not adequate as permanent magnetism will aggregate the MDEBs, preventing them from being evenly dispersed. This is why SPIONs are usually used inside MDEBs [16]. Although SPIONs themselves are not magnetic, once placed in an MRI scanner, they can be magnetized because of the presence of B0 and thus can be visible as magnetic objects from MR images [49]. Moreover, after the particles

leave the magnetic field, their magnetization will disappear. The MDEBs will be released from the aggregates and will reach smaller vessels closer to the tumor areas.

For clinical 3T MRI, the gradient strength is generally smaller than 43 mT/m. Increasing the concentration of SPIONs can generate more magnetic force on MDEBs. However, the con- centration of SPIONs in the current MDEBs has reached 50%. Further increasing this value may encounter technical problems in MDEB fabrication and also reduce the drug-loading [40]. Using materials with higher magnetic magnetization may face biocompatibility issues [50].

For swine#1, the same MRN method (left direction, see Fig. 3(b)) was used for the first two injections. Injected particle aggregates have a 5%–15% breaking rate which is the char- acteristic of our injection system [24]. We found that the first injected aggregate was broken. Since the MRI gradients affect the whole field, the broken aggregate fragments can still move towards the targeted blood vessel under the action of the MRN force. As the blood flow rate was reduced (<1 ml/s) when the particle aggregates were injected, the broken fragments stayed at different locations of the targeted blood vessel or different sub-branches of the targeted blood vessel. When we injected the second particle aggregate, following embolization, it was aggregated with two fragments of the first injection. This is a normal phenomenon and does not have a negative impact on MRN. However, in multi-bifurcation MRN, we must reduce the breaking rate of the injected aggregates to increase the targeting efficiency.

B. The AVC-PC Relationship

We studied the effect of the experimental and imaging parameters (phantom orientation to B0, BW and TE) on the AVC-PC relationship. In the glass phantom, we found that the orientation of the phantom did not affect the relationship because the long axis of MDEB aggregates remained aligned with B0 despite phantom rotation. The shape of the aggregates also did not change with the rotation of the phantom. This directional characteristic is a normal physical phenomenon in MRI [51]. In theory, increasing the BW can minimize artifact size [52]. As the BW increases, the geometric distortion and intravoxel phase dispersion induced by magnetic objects can decrease in the total MR imaging signal, thereby reducing the image distortion and the corresponding artifact volume [52]. However, in our experiments, changing the BW at the fixed TE = 2.5 ms has not been found to have a significant effect on the artifact volume. These observations are similar to those seen by Port et al. [29]. In their work, the BW settings on the MR scanner did not vary significantly and this was the reason why they also did not observe the theoretical phenomenon that the BW can affect the artifact volume. The maximum BW value in their selections was about 1.5 times (15.6/10.4) bigger than the minimum value and the ratio was similar with our BW selections (980/630 = 1.56, Fig. 7(b)). A shorter TE can induce less time for intravoxel phase dispersion to occur before the echo is regenerated, thereby reducing the artifact volume [29]. We confirmed the theoretical effect of TE in our experiments. This also explains why the out-of-phase contrast images

(TE = 1.4 ms) have a smaller artifact size than the in-phase images (TE = 2.6 ms), as shown in Fig. 5(b).

C. SNR and the Background Signal b

Directly studying the distribution of SNRs in the liver might be a more effective way to determine the distributions of b in the 3D space. While MDEB aggregates were surrounded by blood vessels (blood inside, SNR = 174.1) and surrounding liver tissues (SNR = 300.6), the particles used in the in vitro experiments were surrounded by PVA (SNR = 400.2) or glass (SNR = 67.2), and water. By comparing these three objects (liver, PVA phantom, glass phantom), we found that their b values (b = [58-67] in the liver, 70.5 in the glass phantom, and 5.7 in the PVA phantom) will increase with the SNR values.

Signal loss inside vessels can be caused by spin dephasing due to blood flow, which means that the SNR values of blood flow may also affect b. However, the T1-VIBE sequence with a short TE is less susceptible to spin dephasing.

D. Choosing the Best Threshold Range In Vivo

The W/L was just to observe the boundary of the artifact areas more intuitively. The threshold value set in the post-processing software was determined to automatically select the artifact areas with complete coverage. We initially selected four different threshold ranges [0, 140], [0, 160], [0, 180] and [0, 200] when using glass and PVA phantoms. Within these four ranges, the artifact areas can be automatically localized. A larger threshold range (> [0, 200]) will cause some areas (close to artifact areas) to be automatically selected, causing interference. If the threshold is too small (< [0, 140]), some artifact areas visible cannot be covered. In Fig. 8(b), values of a obtained in the PVA phantom and the glass phantom were compared when using the four threshold ranges above. In the range [0, 200], values related to the MRI parameters known here as a have the smallest difference (<1%) in the two phantoms. Fig. 8(b) also revealed that changing the background will not change the value of b. This is why we used a = 3.6 and the threshold range [0, 200] directly in the analysis of the in vivo results.

The signal intensity of different regions of the liver varies a lot. However, the SNR of liver tissues has no obvious difference (Section III-E) in the adjacent areas where the particles can reach. The SNR of the adjacent liver tissues (300.6 ± 29.8) was between that of glass wall (67.2) and PVA (400.2) values. There-
fore, the optimal threshold range used for the two phantoms is theoretically applicable to the liver.

E. Limitations of Our Research

The manual segmentation needed for the quantification of MDEBs is still time consuming and subjective. Previously pro- posed automatic segmentation techniques could improve our segmentation approach in the future [53], [54].

The hepatic vascular tree was subject to deformation (see Fig. 11(b)) from gravity after the possible posture change of the swine, from the phase difference when doing the breath-hold and from body bulk motion, which provides misalignment in the MRA-DSA vascular tree. For swine#2, the pig was positioned in the same supine position between the MRA and DSA acquisitions using a docking table. A better alignment of vascular structures between both modalities was observed (Figs. 11(b) and 12(b)). The intrinsic susceptibility of the liver challenges the selection of the correct artifact areas induced by MDEBs. We used the VIBE to reduce motion artifacts. Moreover, MR imaging was performed before (Fig. 9(a)) and after (Fig. 9(b)) MDEB injection, which helped to distinguish the particle artifacts by comparing the MR images at the same slice position.
We have aimed to accurately locate and quantify MDEB aggregates in the liver. For the two aggregates steered with MRN, they successfully reached the targeted areas (left lobe). The nineteen aggregates injected without steering went naturally to the right lobe (see Fig. 10(a) and (c)). In the future, more particles will be navigated to verify the effectiveness of the MRN steering.

The method used to calculate the SNR is a single image evaluation method. The T1-VIBE sequence used partially parallel imaging, known as CAIPIRINHA (acceleration factor = 4). In partially parallel imaging, SNR values obtained using the single image method are often inaccurate [48]. To verify the effective- ness of the chosen SNR method, the geometry factor (g-factor) ≥ 1 should be obtained [48]. Previous research results indicate that the g-factor is about 0.85 for mSENSE reconstruction and 0.59 for GRAPPA reconstruction when using this SNR method at acceleration factor =2 [48]. The CAIPIRINHA acquisition uses phase offset to improve the accuracy of reconstruction while reducing noise and aliasing, which is a post-processing method that the previous two reconstruction technologies do not have. This can increase the value of the g-factor and thus improve the accuracy of our selected SNR method [55]. In future studies, complex but more accurate SNR calculation methods are recommended.

F. Potential Applications

The technique presented herein has the potential to become a standard method of accurately quantifying and localizing MDEBs after using different types of magnetic targeting methods or techniques, such as MRN and dipole field navigation [20], [56], [57]. Moreover, even for other non-magnetic navigation methods or traditional particle-based transcatheter arterial chemoembolization, the technique can be an intra-and post-procedural assessment method if SPIONs are encapsulated into the MDEBs. A concentration of 50% SPIONs was enough to provide a sufficient steering force to direct the particles to the desired locations [20]. However, for other embolization methods, the concentration value can be decreased to obtain a larger drug-loading. MRI visibility of the MDEBs encapsulating fewer SPIONs needs to be assessed.

V. CONCLUSION

Quantification and 3D localization of drug-eluting micro- robots in deep tissues remain relatively unexplored. We pro- vided a proof of concept, demonstrating that T1-VIBE-

based susceptibility artifacts can be used to accurately localize and quantify SPIONs-based MDEB aggregates. We fabricated typi- cal MDEBs composed of PLGA and Fe O SPIONs coated with C12-bisphosphonate. By defining the W/L and threshold values in the post-processing software, the selection of the artifact areas was fast and accurate. The relationship between the artifact voxel count and the particle count was explained and validated through in vitro and in vivo experiments. Our results revealed that the proposed estimation method had enough accuracy to identify individual MDEBs in the body. We also accurately calculated the number of particles in each aggregate according to the number of segmented voxels in each aggregate artifact. Furthermore, given that the T1-VIBE sequence can be used to form high-quality multiplanar and 3D reconstruction images, the position of the injected MDEBs can be accurately localized. Combining MRA with DSA provided a more intuitive analysis of the particle distribution. Both particle quantification and localization were validated in the livers of two living swine.

REFERENCES

[1] X. Lu et al., “A human microrobot interface based on acoustic manipula- tion,” ACS Nano, vol. 13, pp. 11443–11452, 2019.

[2] L. Yang et al., “An automated microrobotic platform for rapid detection of c. diff toxins,” IEEE Trans. Biomed. Eng., vol. 67, no. 5, pp. 1517–1527, May 2020.

[3] M. Latulippe et al., “Enabling automated magnetic resonance imaging- based targeting assessment during dipole field navigation,” Appl. Phys. Lett., vol. 108, 2016, Art. no. 062403.

[4] T.-A. Le, M. P. Bui, and J. Yoon, “Electromagnetic actuation system for focused capturing of magnetic particles with a half of static saddle potential energy configuration,” IEEE Trans. Biomed. Eng., vol. 68, no. 3, pp. 869–880, Mar. 2021.

[5] X. Yan et al., “Multifunctional biohybrid magnetite microrobots for imaging-guided therapy,” Sci. Robot., vol. 2, 2017, Art. no. eaaq1155.

[6] Z. Zhang et al., “Robotic micromanipulation: Fundamentals and appli- cations,” Annu. Rev. Control, Robot., Auton. Syst., vol. 2, pp. 181–203, 2019.

[7] Q. Cai et al., “Specific, Non-invasive, and magnetically directed targeting of magnetic erythrocytes in blood vessels of mice,” IEEE Trans. Biomed. Eng., vol. 67, no. 8, pp. 2276–2285, Aug. 2020.

[8] B. Wang et al., “Endoscopy-assisted magnetic navigation of biohybrid soft microrobots with rapid endoluminal delivery and imaging,” Sci. Robot., vol. 6, pp. 1–14, 2021, Art. no. eabd2813.

[9] J. Zhang et al., “Liquid crystal elastomer-based magnetic composite films for reconfigurable shape-morphing soft miniature machines,” Adv. Mater., vol. 33, 2021, Art. no. 2006191.

[10] D. Vilela et al., “Medical imaging for the tracking of micromotors,” ACS Nano, vol. 12, pp. 1220–1227, 2018.

[11] J. Zhang et al., “Voxelated three-dimensional miniature magnetic soft machines via multimaterial heterogeneous assembly,” Sci. Robot., vol. 6, 2021, Art. no. eabf0112.

[12] I. Ouedraogo, “Etude de l’anatomie artérielle hépatique chez des patients a eints de CHC, pour un traitement par chimioembolisation par navigation par résonance magnétique,” M.S. thesis, UFR Sciences et Techniques, Nantes, 2019.

[13] A. Hong et al., “Real-time holographic tracking and control of micro- robots,” IEEE Robot. Automat. Lett., vol. 2, no. 1, pp. 143–148, Jan. 2017.

[14] E. S. Olson et al., “Toward in vivo detection of hydrogen peroxide with ultrasound molecular imaging,” Biomaterials, vol. 34, pp. 8918–8924, 2013.

[15] P. Pouponneau et al., “Co-encapsulation of magnetic nanoparticles and doxorubicin into biodegradable microcarriers for deep tissue targeting by vascular MRI navigation,” Biomaterials, vol. 32, pp. 3481–3486, May 2011.

[16] S. Zheng et al., “Dual tumor-targeted multifunctional magnetic hyaluronic acid micelles for enhanced MR imaging and combined photothermal- chemotherapy,” Colloids Surfaces B: Biointerfaces, vol. 164, pp. 424–435, 2018.

[17] Y. Shi et al., “A piezoelectric robotic system for MRI targeting assess- ments of therapeutics during dipole field navigation,” IEEE/ASME Trans.
[18] J. Li et al., “Micro/nanorobots for biomedicine: Delivery, surgery, sensing, and detoxification,” Sci. Robot., vol. 2, pp. 1–9, 2017, Art. no. eaam6431.
[19] F. Michaud et al., “Selective embolization with magnetized microbeads using magnetic resonance navigation in a controlled-flow liver model,” Med. Phys., vol. 46, pp. 789–799, 2019.
[20] N. Li et al., “Magnetic resonance navigation for targeted emboliza- tion in a two-level bifurcation phantom,” Ann. Biomed. Eng., vol. 47,
pp. 2402–2415, 2019.
[21] D. H. Kim et al., “MRI visible drug eluting magnetic microspheres for transcatheter intra-arterial delivery to liver tumors,” Theranostics, vol. 5,
pp. 477–488, 2015.
[22] V. Iacovacci et al., “High-Resolution SPECT imaging of stimuli- responsive soft microrobots,” Small, vol. 15, 2019, Art. no. 1900709.
[23] F. Yang et al., “Multifunctional self-assembled supernanoparticles for deep-tissue bimodal imaging and amplified dual-mode heating treatment,” ACS Nano, vol. 13, pp. 408–420, 2019.
[24] N. Li et al., “MRI-compatible injection system for magnetic microparticle embolization,” IEEE Trans. Biomed. Eng., vol. 66, no. 8, pp. 2331–2340, Aug. 2019.
[25] S. H. Kim et al., “USPIO enhanced lymph node MRI using 3D multi-echo GRE in a rabbit model,” Contrast Media Mol. Imag., vol. 11, pp. 544–549, 2016.
[26] P. Pouponneau et al., “MR imaging of therapeutic magnetic microcarriers guided by magnetic resonance navigation for targeted liver chemoem- bolization,” Cardiovasc. Interventional Radiol., vol. 37, pp. 784–790, Jun. 2014.
[27] Y. Chiba et al., “Quantification of metal-induced susceptibility artifacts associated with ultrahigh-field magnetic resonance imaging of spinal implants,” JOR Spine, vol. 2, 2019, Art. no. e1064.
[28] A. R. Deipolyi et al., “Safety and efficacy of 70–150 μm and 100–300 μm drug-eluting bead transarterial chemoembolization for hepatocellu- lar carcinoma,” J. Vasc. Interventional Radiol., vol. 26, pp. 516–522, 2015.
[29] J. D. Port and M. G. Pomper, “Quantification and minimization of mag- netic susceptibility artifacts on GRE images,” J. Comput. Assist. Tomogr., vol. 24, pp. 958–964, 2000.
[30] A. D. Elster, “Sellar susceptibility artifacts: Theory and implications,”
Amer. J. Neuroradiol., vol. 14, pp. 129–136, 1993.
[31] H. Chandarana et al., “Free-breathing radial 3D fat-suppressed T1- weighted gradient echo sequence: A viable alternative for contrast- enhanced liver imaging in patients unable to suspend respiration,” Invest. Radiol., vol. 46, pp. 648–653, 2011.
[32] F. M. Vogt et al., “Parallel acquisition techniques for accelerated volumet- ric interpolated breath-hold examination magnetic resonance imaging of the upper abdomen: Assessment of image quality and lesion conspicuity,”
J. Magn. Reson. Imag.: An Official J. Int. Soc. Magn. Reson. Med., vol. 21,
pp. 376–382, 2005.

[33] E. Koh, E. R. Walton, and P. Watson, “VIBE MRI: An alternative to CT in the imaging of sports-related osseous pathology?,” Brit. J. Radiol., vol. 91, 2018, Art. no. 20170815.
[34] M. C. Mascolo, Y. Pei, and T. A. Ring, “Room temperature co-precipitation synthesis of magnetite nanoparticles in a large pH window with different bases,” Materials, vol. 6, pp. 5549–5567, 2013.
[35] M. Lecouvey et al., “A mild and efficient one-pot synthesis of 1- hydroxymethylene-1, 1-bisphosphonic acids. Preparation of new tripod ligands,” Tetrahedron Lett., vol. 42, pp. 8475–8478, 2001.
[36] C. Zhang and C. Shi, “Superparamagnetic iron oxide nanaoparticles for in vivo stem cell tracking,” Exp. Hematol., vol. 37(Suppl 1), p. 102, 2009.
[37] J. S. Weinstein et al., “Superparamagnetic iron oxide nanoparticles: Diag- nostic magnetic resonance imaging and potential therapeutic applications in neurooncology and central nervous system inflammatory pathologies, a review,” J. Cereb. Blood Flow Metab., vol. 30, pp. 15–35, 2010.
[38] D. Barati et al., “Injectable and crosslinkable PLGA-Based microribbons as 3D macroporous stem cell niche,” Small, vol. 16, 2020, Art. no. 1905820.
[39] B. C. Odisio et al., “Transarterial hepatic chemoembolization with 70–150 μm drug-eluting beads: Assessment of clinical safety and liver toxicity profile,” J. Vasc. Interventional Radiol., vol. 26, pp. 965–971, 2015.
[40] Z. Nosrati et al., “Development of a coflowing device for the size- controlled preparation of magnetic-polymeric microspheres as emboliza- tion agents in magnetic resonance navigation technology,” ACS Biomate- rials Sci. Eng., vol. 4, pp. 1092–1102, 2018.
[41] S. B. Gay et al., “Breath-holding capability of adults: Implications for spi- ral computed tomography, fast-acquisition magnetic resonance imaging, and angiography,” Invest. Radiol., vol. 29, pp. 848–851, 1994.
[42] R. Kikinis, S. D. Pieper, and K. G. Vosburgh, “3D Slicer: A platform for subject-specific image analysis, visualization, and clinical support,” in Intraoperative Imaging and Image-Guided Therapy, Springer, 2014,
pp. 277–289.
[43] W. Zhou et al., “Grayscale contrast enhancement based on greyscale-based contrast-to-noise ratio,” in Proc. Med. Imag. 2021: Image Percep., Ob- server Perform., Technol. Assessment, 2021, Art. no. 1159907.
[44] F. Zehtabi et al., “Chitosan–sodium tetradecyl sulfate hydrogel: Char- acterization and preclinical evaluation of a novel sclerosing embolizing agent for the treatment of endoleaks,” Cardiovasc. Interventional Radiol., vol. 40, pp. 576–584, 2017.

[45] C. Tous et al., “Navigation of microrobots by MRI: Impact of gravitational, friction and thrust forces on steering success,” Ann. Biomed. Eng., vol. 49,
pp. 3724–3736, 2021.
[46] M. Gérard et al., “Geometric modeling of hepatic arteries in 3D ultrasound with unsupervised MRA fusion during liver interventions,” Int. J. Comput. Assist. Radiol. Surg., vol. 12, pp. 961–972, 2017.

[47] R. M. Henkelman, “Measurement of signal intensities in the presence of noise in MR images,” Med. Phys., vol. 12, pp. 232–233, 1985.
[48] F. L. Goerner and G. D. Clarke, “Measuring signal-to-noise ratio in partially parallel imaging MRI,” Med. Phys., vol. 38, pp. 5049–5057, 2011.
[49] S. Martel, “Beyond imaging: Macro-and microscale medical robots actuated by clinical MRI scanners,” Sci. Robot., vol. 2, 2017, Art. no. eaam8119.
[50] P. Singh et al., “FeCo nanoparticles as antibacterial agents with improved response in magnetic field: An insight into the associated toxicity mecha- nism,” Nanotechnology, vol. 32, 2021, Art. no. 335101.
[51] J.-B. Mathieu and S. Martel, “Aggregation of magnetic microparticles in the context of targeted therapies actuated by a magnetic resonance imaging system,” J. Appl. Phys., vol. 106, 2009, Art. no. 044904.
[52] J. R. Reichenbach et al., “Theory and application of static field inhomo- geneity effects in gradient-echo imaging,” J. Magn. Reson. Imag., vol. 7,
pp. 266–279, 1997.
[53] M. R. Avendi, A. Kheradvar, and H. Jafarkhani, “Automatic segmentation of the right ventricle from cardiac MRI using a learning-based approach,” Magn. Reson. Med., vol. 78, pp. 2439–2448, 2017.
[54] X. Alba et al., “Automatic cardiac LV segmentation in MRI using modified graph cuts with smoothness and interslice constraints,” Magn. Reson. Med., vol. 72, pp. 1775–1784, 2014.
[55] S. R. Yutzy et al., “Improvements in multislice parallel imaging us- ing radial CAIPIRINHA,” Magn. Reson. Med., vol. 65, pp. 1630–1637, 2011.
[56] M. Latulippe and S. Martel, “Dipole field navigation: Theory and proof of concept,” IEEE Trans. Robot., vol. 31, no. 6, pp. 1353–1363, Dec. 2015.
[57] C. Zhou et al., “Engineering micromotors with droplet microfluidics,” ACS Nano, vol. 13, pp. 6319–6329, 2019.

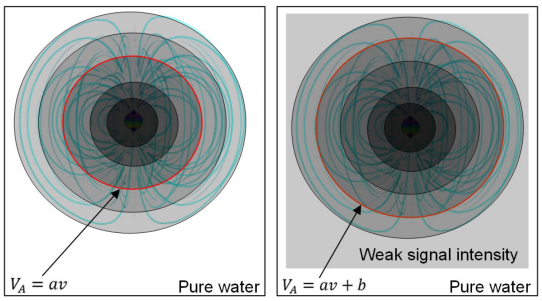

Fig. 1. A sketch to show the different relationships between the particle volume and the artifact volume without (a) and with (b) weak background signal intensity. Note, the red line indicates the boundary of the signal dropout regions that can be identified.

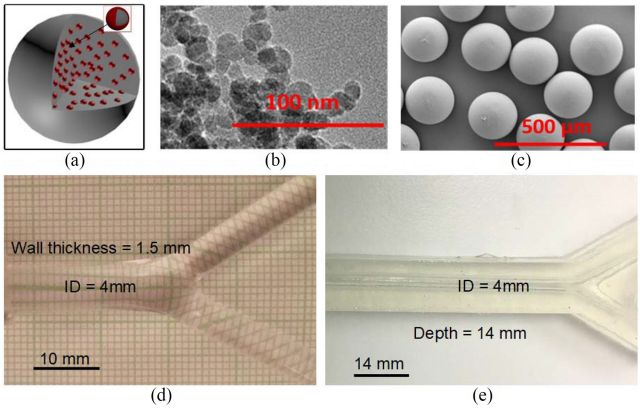

Fig. 2. MDEBs and in-vitro phantoms used in the experiments. (a) Schematic diagram of the synthesized PLGA-based-MDEB encapsulating Fe3O4 nanoparticles coated with C12-bisphosphonate (red surface).
(b) Transmission electron microscopy micrograph of the Fe3O4 nanoparticles. (c) Scanning electron microscope image of the MDEBs. (d) and
(e) show the photos of the glass (d) and the PVA (e) phantoms. Note: In
(c) and (d), ID = internal diameter.

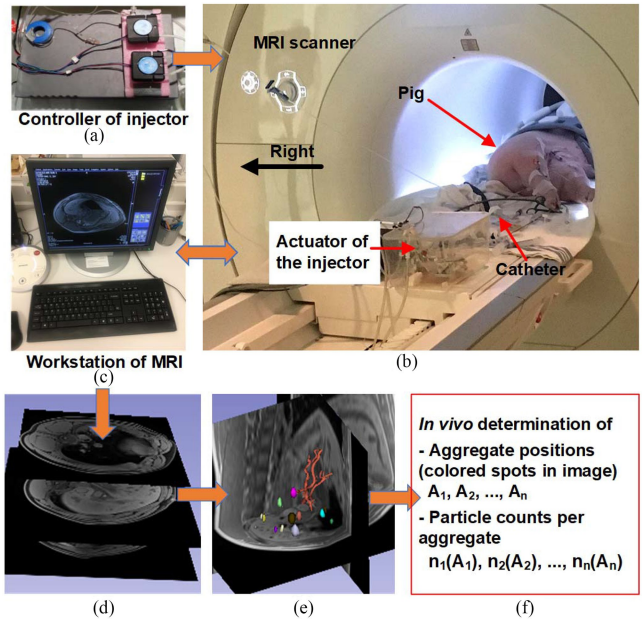

Fig. 3. Schematic representation of the workflow from MDEB MRN (a–c) to quantification and 3D localization (d-f) of the MDEBs in the swine liver. (a) The MDEB aggregates were formed in a particle injection system. (b) The catheter, inserted into the hepatic artery of a living swine, was connected to the MRI-compatible injection system to allow the injection of the MDEB aggregates into the proximal proper hepatic artery. (c) MRI workstation controlled the MRN sequence and received the T1-VIBE-based MR images. (d–f) The proposed post-processing method, based on the T1-VIBE-based susceptibility artifact reconstruction, was used to quantify and locate MDEB aggregate fragments located throughout the liver.

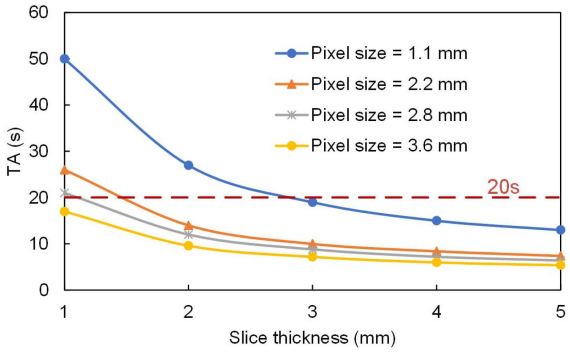

Fig. 4. TA with different slice thicknesses and pixel sizes.

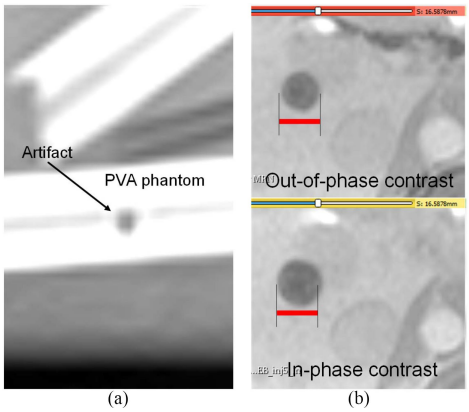

Fig. 5. (a) A single MDEB is clearly visible in the PVA phantom using the T1-VIBE sequence. (b) Images showing that the out-of-phase con- trast images (up) can have a smaller MDEB-induced artifact compared with the in-phase contrast images (down) when using the T1-VIBE sequence. Note, in (b), 1) the images are from the following in vivo experiment, 2) the two images are enlarged at the same scale at the same time before taking the screenshot, and 3) the red lines in the two images have the same length.

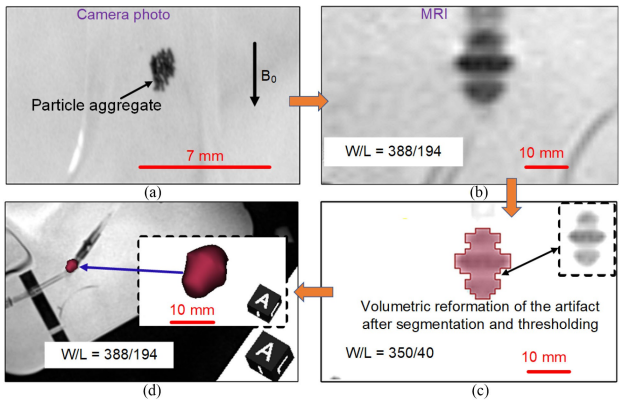

Fig. 6. Flowchart showing how to obtain the artifact volume from MR imaging. (a) Photograph of a 60-particle aggregate in the glass phantom inside the MRI bore. (b) MR imaging of the aggregate artifact using the default imaging parameters. (c) Segmentation of the aggregate artifact.
(d) 3D reconstruction of aggregate segmentation.

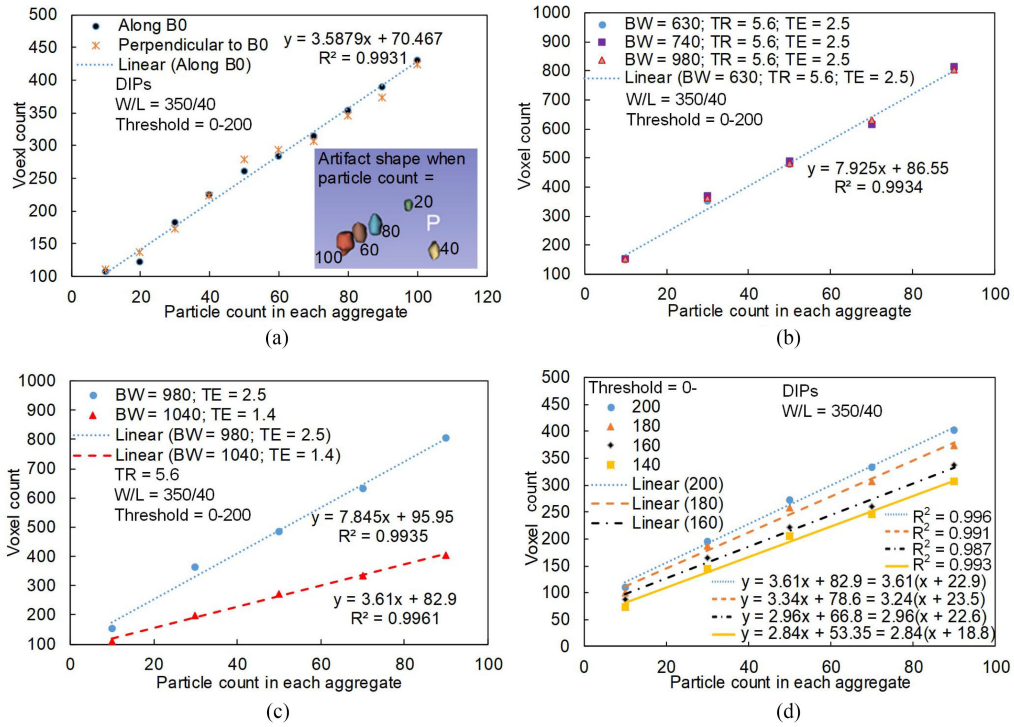

Fig. 7. The AVC-PC relationship in the glass phantom according to orientation to B0, BW, TE and segmentation threshold. (a) The main branch of the phantom was positioned inside the MRI along and perpendicular to B0. (b) Particle count versus artifact voxel count when BW = 630, 740, 980, and 1040 Hz. (c) Particle count versus artifact voxel count when using different BW (980 and 1040 Hz) and TE values (1.4 ms and 2.5 ms). (d) Particle count versus artifact voxel count when the threshold range of the segmentation software was set to different values. Note that 1) all TR and TE values in Figures are in ms, and BW values in Hz, and 2) all parameters in this manuscript were evaluated using the out-of-phase reconstruction of the VIBE sequence. Note, in (a) and (d), the DIPs are the default imaging parameters defined in Section III-A.

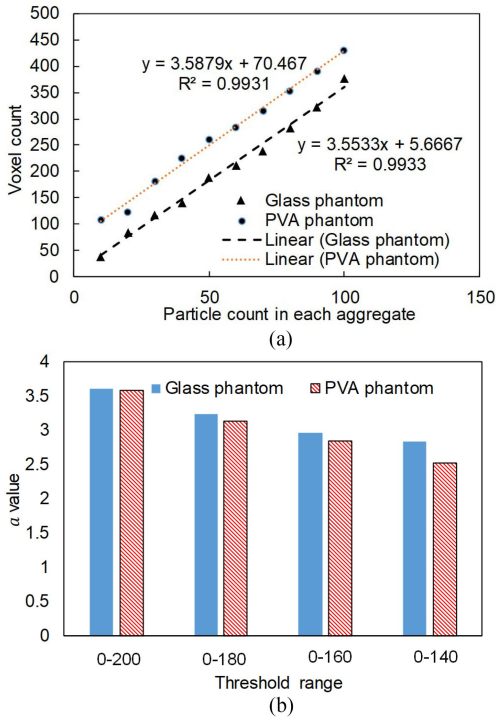

Fig. 8. Relationship between the particle count and the corresponding artifact voxel count in the glass phantom and the PVA phantom. (a) Relationship equations when only changing phantoms. (b) Values of a in the PVA phantom and the glass phantom, when using different threshold ranges in the post-processing software.

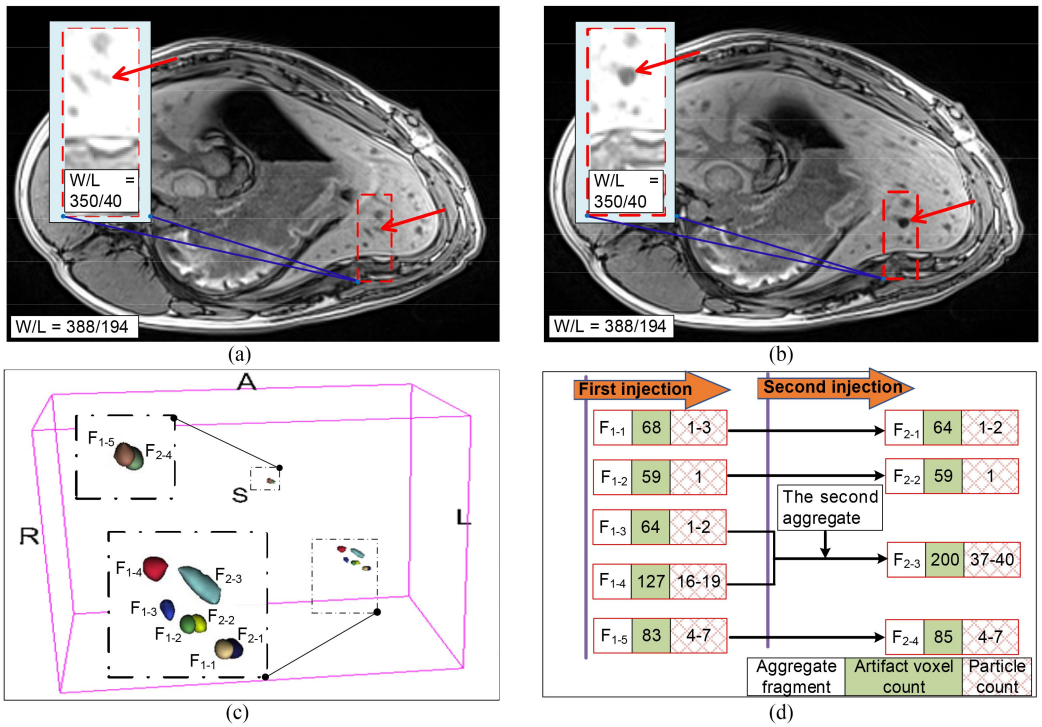

Fig. 9. Quantification of particles in the liver of a living swine. In vivo identification of an MDEB aggregate artifact in the liver by comparing MR images obtained (a) before and (b) after injection. (c) 3D distribution of artifacts from fragmented particle aggregates after the first two injections.
(d) Statistics of particle count in each fragment after the first two injections and using Eq. 3, a = 3.6 and b = 58-67 (see text).

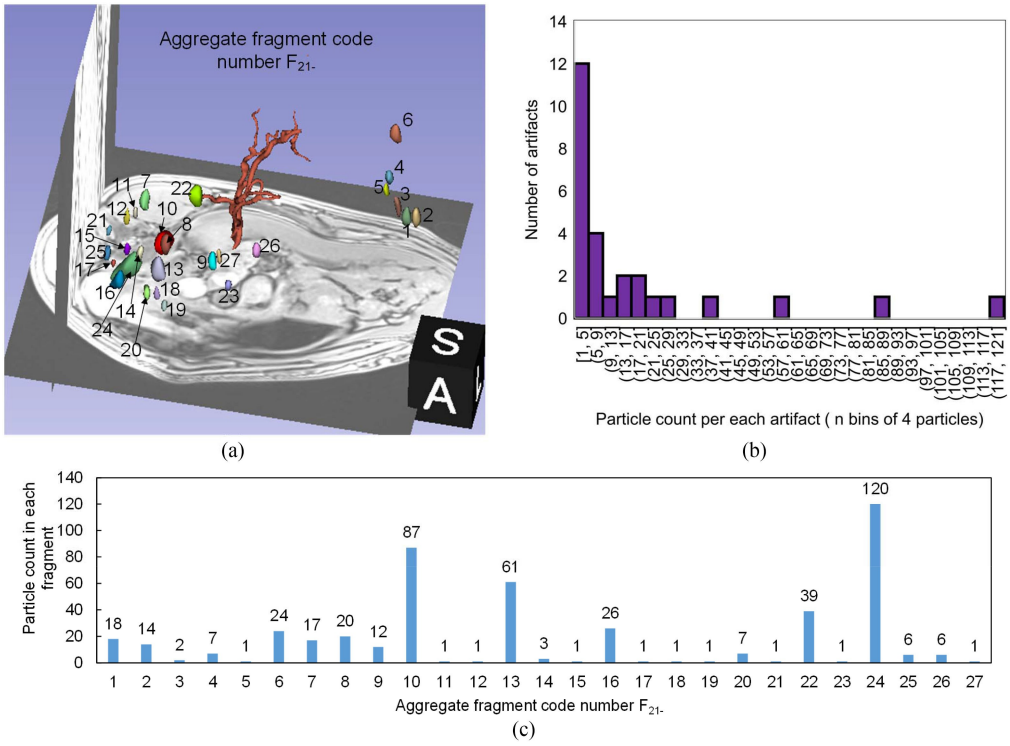

Fig. 10. In vivo identification of MDEB artifacts in the liver after injecting 21 aggregates and performing MRA of hepatic arteries. (a) 3D locations of MDEB fragments with the MRA of hepatic arteries. (b) After injecting 21 aggregates and then calculating the number of particles in each aggregate fragment using Eq. (3), a = 3.6 and b = 60, the distribution range of the number of particles is counted in different aggregate fragments. The code number of the aggregate fragments has been marked in (a). (c) Number of particles in each aggregate fragment after injecting 21 aggregates.

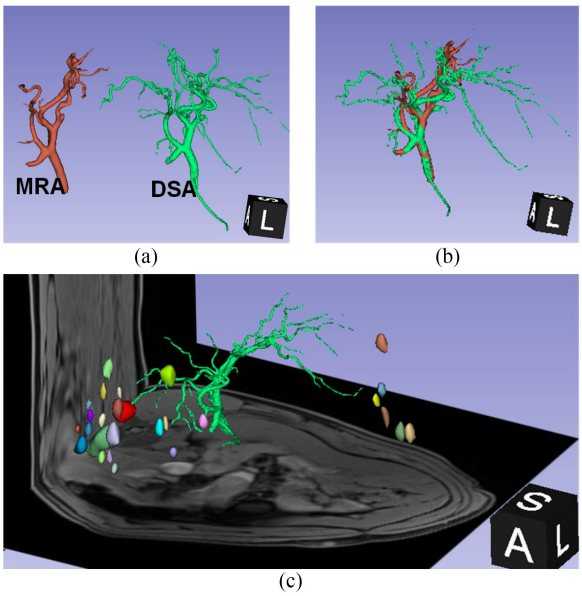

Fig. 11. Localization of aggregate fragments in the liver of swine#1.
(a) Hepatic arterial tree obtained by MRA and DSA. The hepatic tree obtained by DSA is in green to facilitate identification. (b) Coordinate alignment of the MRA and DSA images clearly displays the deformation of the hepatic vascular tree. Both images were segmented in the 3D slicer. The DSA image was manually loaded into Fig. 10a, and then manually aligned with the MRA image as much as possible by referring to the location of main branches and left-and right-hepatic arteries. (c) Identification of MDEB artifacts after inserting DSA of hepatic arteries.

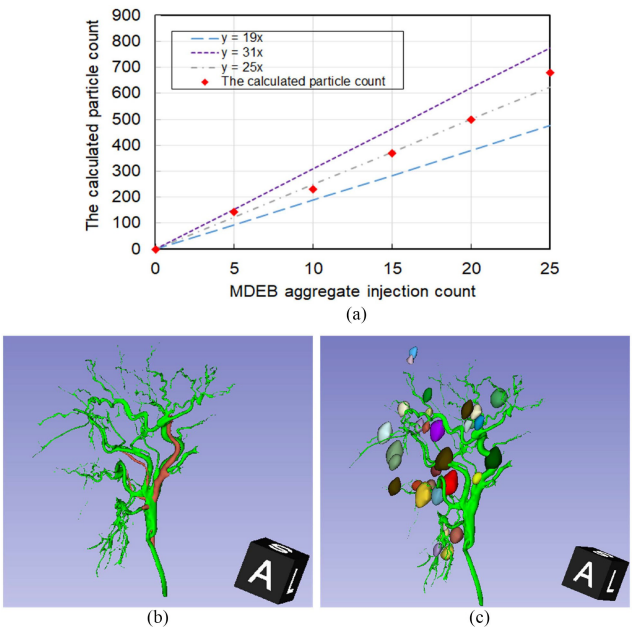

Fig. 12. Quantification and 3D localization of MDEBs injected into the liver of Swine#2. (a)The calculated particle count versus the MDEB aggregate injection count. (b) Coordinate alignment of the MRA (red) and DSA (green) images of the hepatic vascular tree. (c) Identification of MDEB artifacts after inserting DSA of hepatic arteries. Note, in (a), y = 19x, y = 31x and y = 25x respectively indicate the upper limit, the lower limit, and the average value of the theoretical injection precision through our injection system.